Journal of Geophysical Research: Space Physics

RESEARCH ARTICLE

10.1029/2018JA025338

Transmission of a Magnetospheric Pc1 Wave Beam Through the Ionosphere to the Ground

E. N. Fedorov[1], **V. A. Pilipenko**[1,2], **M. J. Engebretson**[3], and **M. D. Hartinger**[4]

[1]Institute of Physics of the Earth, Moscow, Russia, [2]Space Research Institute, Moscow, Russia, [3]Center for Atmospheric and Space Sciences, Augsburg University, Minneapolis, MN, USA, [4]Department of Electrical and Computer Engineering, Virginia Polytechnic Institute and State University, Blacksburg, VA, USA

Key Points:
- Transmission of magnetospheric Pc1 Alfven wave beam through the ionosphere to the ground has been numerically modeled
- Ionospheric Alfven resonator and fast-mode waveguide ensure dependence of ionospheric transmission/reflective properties on frequency
- Transmission has oscillatory dependence on frequency, forming transmission windows at resonant frequencies of resonator and waveguide

Correspondence to:
V. A. Pilipenko,
space.soliton@gmail.com

Citation:
Fedorov, E. N., Pilipenko, V. A., Engebretson, M. J., & Hartinger, M. D. (2018). Transmission of a magnetospheric Pc1 wave beam through the ionosphere to the ground. *Journal of Geophysical Research Space Physics*, *123*, 3965–3982. https://doi.org/10.1029/2018JA025338

Received 9 FEB 2018
Accepted 31 MAR 2018
Accepted article online 4 APR 2018
Published online 2 MAY 2018

Abstract

A characteristic feature of the upper ionosphere is the occurrence of the ionospheric Alfvén resonator (IAR) and the ionospheric fast-mode waveguide (IFW), which can trap electromagnetic wave energy in the Pc1 frequency range from fractions of a hertz to a few hertz. This wave trapping ensures the dependence of ionospheric transmission/reflective properties on frequency. We numerically model magnetospheric Alfvén wave transmission through the ionosphere to the ground based on solution of the magnetohydrodynamic full-wave equations in a realistic ionosphere, whose parameters are reconstructed from the International Reference Ionosphere model. The spatial structure of an incident wave is modeled as a localized beam with a finite latitudinal scale $\lambda_\perp$ and an azimuthally propagating wave. The IAR and IFW modes are coupled owing to the Hall conductivity and geomagnetic field inclination. Ground spatial and spectral structures of the Pc1 wave (0.1- to 6-Hz band) have been calculated for summer day/night conditions at the Antarctic Halley observatory, though results may be qualitatively applied to any midlatitude site. An incident wave with azimuthal wave vector $k_y = 1.7 \cdot 10^{-3}$ km^{-1}, and $\lambda_\perp = 10^2$ km has been considered. The model predicts that beneath the incident beam the ground magnetic response "duplicates" its structure after accounting for a $\pi/2$ rotation and some latitudinal shift/widening. The transmission has an oscillatory dependence on frequency, thus forming "transmission windows" at resonant frequencies of IAR and IFW modes. The spectra vary depending on distance from an incidence point. Interference between IFW modes is revealed in the nonmonotonic and frequency-dependent character of latitudinal variations of wave amplitude.

1. Introduction: Pc1 Waves and Transmission/Reflective Properties of the Ionosphere

Electromagnetic ion cyclotron (EMIC) waves in the Pc1 band (from 0.1 Hz to several hertz), generated by resonant wave-particle interactions, are an important factor of space weather in the near-Earth environment. These waves may account for a depletion of MeV-electron fluxes in the radiation belt (Lyons & Thorne, 1972; Shprits et al., 2008; Ukhorskiy et al., 2010), limit the life time of energetic ring current protons (Kennel & Petschek, 1966), and produce localized proton aurora (Yahnin et al., 2007). The temperature anisotropy necessary for the instability may increase due to either betatron acceleration upon injection of ring current protons into the inner magnetosphere (Daglis et al., 1999) or solar wind pressure increase pulses (Arnoldy et al., 2005). Both mechanisms preferentially increase the ion energy perpendicular to the background magnetic field. Once generated, these waves propagate along magnetic field lines, reaching the ionosphere and providing a ground signal. Near-equatorial spacecraft observed EMIC wave activity throughout the magnetosphere, up to high geomagnetic shells, $L \simeq 9$ (Anderson et al., 1992; Keika et al., 2013). Upon the field-aligned propagation in an inhomogeneous magnetosphere EMIC waves are converted from a quasi-parallel regime (when the effective transverse wave vector $k_\perp < k_\parallel^* = k_\parallel(\omega/\Omega)$, where Ω is the ion gyrofrequency and $k_\parallel$ is the field-aligned wave vector) to a quasi-transverse regime (when $k_\perp > k_\parallel^*$; Leonovich et al., 1983). As a result, an EMIC wave packet impinges on the ionosphere as a localized beam across $\mathbf{B}_o$.

To characterize the EMIC activity in the magnetosphere from ground observations, a relevant theoretical model must indicate a possible distortion of Pc1 wave amplitude and spectral content upon the transmission through the ionosphere. For low-frequency (Pc3-5 and Pi2) pulsations the approximation of a thin sheet ionosphere may be used for the description of magnetospheric magnetohydrodynamic (MHD) wave interactions with the ionosphere (Alperovich & Fedorov, 2007). However, this approximation cannot be used for MHD waves in the Pc1 frequency band, whose field-aligned wavelength is of the order of the vertical scale of ionospheric inhomogeneity. The multilayered ionosphere-atmosphere-Earth system supports MHD waveguides and resonators, which can trap electromagnetic waves with frequencies from fractions of a hertz to a few tens of hertz: the ionospheric Alfvén resonator (IAR; Belyaev et al., 1990; Lysak, 1997), the ionospheric fast-mode waveguide (IFW; Fujita & Tamao, 1988; Greifinger & Greifinger, 1968), and the Earth-ionosphere waveguide for electromagnetic waves (Kikuchi & Hashimoto, 2016). In an inhomogeneous ionosphere with anisotropic conductivity and inclined magnetic field the ionospheric MHD modes and atmospheric electromagnetic waves are mutually coupled. The coupling rate strongly depends on the transverse wave number, or, in other words, on the angle of the wave incidence. The IAR has been intensively studied both theoretically and experimentally. Ground IAR signatures (multiple spectral bands separated by the frequency scale $\Delta f \sim 0.3-0.5$ Hz) have been found during nighttime hours at low, middle, auroral latitudes and even poleward from the auroral oval (see relevant references in the reviews by Demekhov, 2012; Lysak & Yoshikawa, 2013; Pilipenko, 2012; Surkov & Hayakawa, 2014). In winter the IAR signatures can be seen round the clock (Potapov et al., 2014).

Within the ionosphere, an EMIC wave is partially converted to a ducted IFW mode that can be carried thousands of kilometers relative to the locations of the wave injection into the ionosphere (Fraser et al., 2006; Kim et al., 2010, 2011). Observations of Pc1 structured emissions at widely separated stations were interpreted by Potapov et al. (2002) as an evidence of the possibility of very distant ($>10^4$ km) transequatorial propagation along the ionospheric waveguide. The horizontal duct propagation is most efficient along the magnetic meridian (Greifinger & Greifinger, 1973). Thus, the ionosphere operates as an enormous "receiving antenna" collecting magnetospheric EMIC signals from a large area around a ground observer. Ground observations using a search coil magnetometer array (Hayashi et al., 1981; Kim et al., 2010) found that Pc1 waves propagating from an injection region decreased in intensity in a specific way: their attenuation was very rapid ($\sim$10 dB/100 km) in the injection center but became much weaker ($\sim$2.5 dB/100 km) in the region beyond about 500 km from the center.

The resonant properties of the ionosphere ensure the dependence of the Pc1 transmission/reflection properties on frequency (Fedorov, Mazur, Pilipenko, & Engebretson, 2016; Ostapenko & Polyakov, 1990). Frequency-dependent transmission through the ionosphere was suggested to control the Pc1 frequency band observed on the ground (Fraser-Smith, 1987). Indeed, the central frequency of Pc1 emissions was found to correspond to the maximum of the transmission coefficient, coinciding with the frequency of IAR harmonics (Feygin et al., 1994; Mursula et al., 2000; Prikner et al., 2001, 2004). Thus, the ionosphere with the IAR and IFW can act as a multiband band-pass filter for EMIC waves, forming the spectral structure of Pc1 emissions observed on the ground.

For the interpretation of basic features of the EMIC wave interaction with the ionosphere most theoretical models approximated the Alfvén speed $V_A(z)$ in the ionosphere by different analytic functions. Demekhov et al. (2000) used an analytically solvable approximation for the refractive index $n_A(z)$ in the upper ionosphere derived from the International Reference Ionosphere (IRI) model, while the bottom ionosphere was replaced by a thin layer with height-integrated Pedersen and Hall conductances, Σ_P and Σ_H. At the same time, the coupling of Alfvén and IFW modes was neglected. In a generalized model of the IAR Lysak (1993) modeled the ionospheric ion distribution with exponential functions along a flux tube in a dipole magnetic field. At the lower ionosphere boundary an impedance type condition was imposed. The evaluated reflection coefficient exhibited a resonant structure with minima at frequencies corresponding to the IAR modes. Rapid fall of the plasma density just above the ionosphere was shown to be the critical factor in determining the mode frequencies. Ostapenko and Polyakov (1990) indicated that the Alfvén wave reflection coefficient is determined by the combined influence of two resonant structures: IAR and IFW, coupled owing to the Hall conductivity of the ionosphere and oblique geomagnetic field. However, in their modeling the backward influence of the IFW mode on the Alfvén wavefield was neglected.

Peculiarities of the Alfvén wave reflection from the ionosphere cannot be directly used to interpret ground observations. The ground response to the incident Alfvén wave is produced by the secondary fast mode, emerging owing to mode coupling in the anisotropically conducting ionosphere (Alperovich & Fedorov, 2007). This evanescent mode only weakly influences the Alfvén wave reflection. Therefore, mode coupling, strongly dependent on the transverse wave scale, can influence considerably the wave transmission through the ionosphere, but not the reflection from it. In most earlier studies devoted to the IAR excitation problem, the accompanying generation of the compressional mode was neglected.

More recent studies treated the problem of EMIC wave transmission through the ionosphere to the ground in a more consistent way. Woodroffe and Lysak (2012) modeled the ground pattern resulting from incidence of a localized coaxial field-aligned current (Model 2 in the appendix) and isotropic propagation of fast waves along the ionosphere with an analytically modeled profile. The ground signals were found to have a complicated polarization structure. The polarization ellipse was strongly elongated along the N-S direction, with a change of ellipticity sense in the center of the wave incidence region.

Fedorov, Mazur, Pilipenko, and Ermakova (2016) developed a numerical model of the magnetospheric Alfvén wave interaction with the ionosphere based on the solution of multifluid MHD full-wave equations in a realistic ionosphere, whose parameters were reconstructed from the IRI model. In Fedorov, Mazur, Pilipenko, and Engebretson (2016) the transmission/reflection coefficients have been calculated for a wave spatial harmonic, characterized by the horizontal wave vector $k_\perp$. On a qualitative basis, a wave beam with transverse scale $\lambda_\perp$ corresponds to a wave harmonic with $k_\perp = \lambda_\perp^{-1}$. The resulting coefficients have turned out to be strongly frequency modulated due to the IAR and IFW resonant features. However, a realistic magnetospheric wave structure $B(x)$ is composed of a continuum of spatial harmonics with spectral amplitudes $B(k_\perp)$. Because the transmission coefficient is scale dependent, the ground structure is a combination of many harmonics (Alperovich & Fedorov, 1992). Moreover, the modeling results presented in Fedorov, Mazur, Pilipenko, and Engebretson (2016) can only be applied to the interpretation of ground observations just beneath the incidence point of magnetospheric Alfvén waves. For the interpretation of observations at distant stations, the trapping of wave energy into the ionospheric waveguide and propagation along it should be considered similar to Fujita and Tamao (1988) and Woodroffe and Lysak (2012).

Adequate interpretation of EMIC wave mechanisms and dynamics demands a realistic model of Alfvén wave interactions with the ionosphere. The model proposed in this paper describes quantitatively the modification of a localized Pc1 wave beam with different frequencies upon transmission through a realistic ionosphere-atmosphere-ground system.

2. Model of Alfvén Wave Beam Interaction With the Ionosphere

2.1. Basic Wave Equations

We use the same model of the magnetosphere-ionosphere-atmosphere-ground system to describe the propagation of MHD waves from the magnetosphere through an inhomogeneous ionosphere to the ground as in Fedorov, Mazur, Pilipenko, and Engebretson (2016; Figure 1). In a Cartesian coordinate system the x, y, and z axes are directed southward, eastward, and upward, respectively. The magnetic inclination (dip angle) of the geomagnetic field $\mathbf{B}_0$ is denoted as I ($I > 0$ in the Northern Hemisphere and $I < 0$ in the Southern Hemisphere; vertical $\mathbf{B}_0$ corresponds to $I = \pm\pi/2$). Additionally, we use a nonrectangular field-aligned coordinate system $\left\{x^1, x^2, x^3\right\}$, where coordinate lines x^3 coincide with magnetic field lines, x^2 is azimuthal, and x^1 is the radial coordinate across L-shells. This coordinate system is related to the Cartesian coordinate system with relationships $x = x^1 + x^3 \cot I$, $y = x^2$, $z = x^3$. Covariant components of the wave electromagnetic field $\{B_1, B_2\}$ and $\{E_1, E_2\}$ coincide with the horizontal components in the Cartesian coordinate system, that is, $E_1 = E_x$, $E_2 = E_y$, and $B_1 = B_x$, $B_2 = B_y$. The medium is assumed to be homogeneous in the horizontal direction, that is, along x and y.

The electromagnetic field can be decomposed into plane harmonics as follows:

$$\{E, B\}(x^1, x^2, x^3) \propto \exp(-i\omega t + ik_1 x^1 + ik_2 x^2). \tag{1}$$

Here $k_\perp = \{k_1, k_2\}$ is the transverse wave vector, composed from the radial k_1 and azimuthal k_2 components.

The wave electric (**E**) and magnetic (**B**) fields are decomposed into two modes. The magnetospheric wavefield is the sum of an Alfvén mode and a fast magnetosonic mode, whereas an electromagnetic disturbance in the atmosphere and ground is composed of a magnetic H-mode and electric E-mode. The E-mode excitation rate by magnetospheric disturbances is determined by the ratio between the ionospheric conductance and the conductivity of the atmosphere integrated over a wave incidence region (Alperovich & Fedorov, 2007). Therefore, only large-scale sources, like interplanetary shocks, can produce a discernible response on the ground

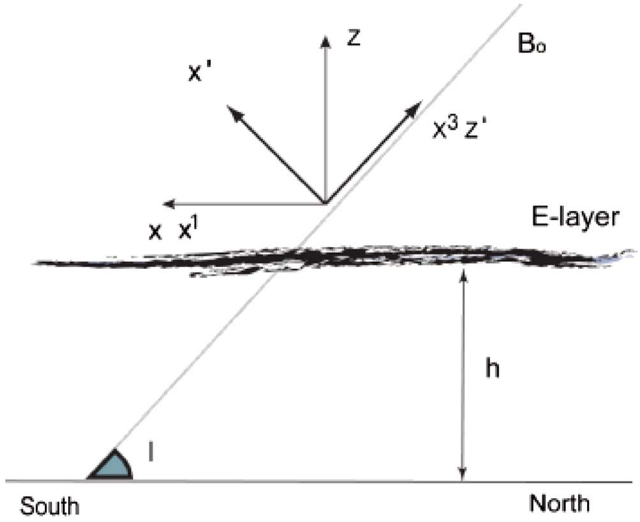

Figure 1. A sketch of the geometry used: Cartesian coordinate system $\{x, y, z\}$, nonrectangular field-aligned coordinate system $\left\{x^1, x^2, x^3\right\}$, and local orthogonal coordinate system $\{x', y', z'\}$. $\mathbf{B}_o$ is the geomagnetic field; I is the field inclination.

(Kikuchi & Hashimoto, 2016). At the same time, the E-mode propagates nearly instantly (with speed comparable to the light velocity) along the ground-ionosphere waveguide and decays little upon propagation, so its contribution to the ground wave structure may only be noticeable at large distances.

The boundary conditions for the electromagnetic field at the ground surface are derived via the spectral surface impedances for E-mode and H-mode. If the wave skin depth $\delta_g = (2/\omega\mu_0\sigma_g)^{1/2}$ in the ground with conductivity σ_g is much less than the horizontal scale, that is, $k_x\delta_g \ll 1$, the electric and magnetic impedances are nearly identical, $Z_g^{(E)} \simeq Z_g^{(H)}$. In this case the boundary condition is as follows:

$$-E_1/B_2 \simeq E_2/B_1 \simeq \mu_0^{-1} Z_g, \tag{2}$$

where μ_0 is the magnetic permeability of free space. The impedance of the homogeneous semispace is $Z_g = \exp(-i\pi/4)\sqrt{\omega\mu_0/\sigma_g}$.

The wave modification upon propagation from the magnetosphere to the ground is determined from the solution of Maxwell's equations in a medium with the complex permittivity tensor $\hat{\varepsilon}$, which in a coordinate system with a $\mathbf{B}_0$-aligned z axis appears as follows:

$$\hat{\varepsilon} = \begin{pmatrix} \varepsilon_\perp & ig & 0 \\ -ig & \varepsilon_\perp & 0 \\ 0 & 0 & \varepsilon_\parallel \end{pmatrix}. \tag{3}$$

The tensor components $\varepsilon_\perp$ and ig are calculated below numerically using the cold collisional plasma approximation (Ginzburg, 1970).

In an oblique coordinate system $\{x^1, x^2, x^3\}$ full-wave equations for the tensor (3) have been derived in Fedorov, Mazur, Pilipenko, and Ermakova (2016). The finite field-aligned conductivity ($\sigma_\parallel \propto \varepsilon_\parallel$) due to electron collisions in the ionosphere produces a diffusion and absorption of electromagnetic wave structures with small transverse scales ≤ 2 km (Lessard & Knudsen, 2001). For Alfvén waves with large horizontal scales, much larger than the skin depth $\delta_\parallel$ determined by the field-aligned conductivity $\sigma_\parallel$, the general system from Fedorov, Mazur, Pilipenko, and Ermakova (2016) reduces to the following set of equations:

$$\begin{aligned}
\partial_3 B_1 &= ik_1 \cot I B_1 + \left(\frac{-ik_1k_2}{\omega} + \frac{\omega\mu_0 g}{\sin I}\right)E_1 + \left(\frac{ik_1^2}{\omega} - i\omega\mu_0\varepsilon_\perp\right)E_2 \\
\partial_3 B_2 &= ik_2 \cot I B_1 + \left(\frac{-ik_2^2}{\omega} + \frac{i\omega\mu_0\varepsilon_\perp}{\sin I^2}\right)E_1 + \left(\frac{ik_1k_2}{\omega} + \frac{\omega\mu_0 g}{\sin I}\right)E_2 \\
\partial_3 E_1 &= i\omega B_2, \qquad \partial_3 E_2 = -i\omega B_1 - ik_2(\cot I)E_1 + ik_1(\cot I)E_2.
\end{aligned} \tag{4}$$

At sufficiently large k_1, when mode coupling owing to the Hall conductivity can be neglected, the system (4) splits into two uncoupled subsystems:

$$\partial_s^2 E_1 + k_A^2 E_1 = 0 \tag{5}$$

for Alfvén waves, where $k_A = \omega\sqrt{\varepsilon_\perp \mu_0} = \omega/V_A$ is the Alfvén wave number, $s = x^3/\sin I$ is the distance along a field line, and $\partial_s = \sin I \partial_3$ and

$$\partial_z^2 E_2 + \left(k_A^2 - k_1^2\right) E_2 = 0 \tag{6}$$

for fast-mode waves, where $\partial_z = \partial_3 - ik_1 \cot I$.

The backward influence of the fast mode on Alfvén wave reflection can be neglected if the horizontal scale of the wave is sufficiently small (Lysak & Yoshikawa, 2013; Yagova et al., 1999), namely,

$$k_\perp \gg k_* = \left(\Sigma_H/\Sigma_P\right)^2 \mu_0 \omega \Sigma_P. \tag{7}$$

The significance of the mode coupling between Alfvén wave and IFW modes in a realistic ionosphere received a special consideration in Fedorov, Mazur, Pilipenko, and Ermakova (2016).

2.2. Spatial Structure of the Incident Alfvén Wave Beam

The electromagnetic field $\mathbf{E}_\perp$, $\mathbf{B}_\perp$, and field-aligned current $j_\parallel$ transported by the Alfvén wave are determined by the wave scalar potential Φ:

$$\mathbf{E}_\perp = -\nabla_\perp \Phi, \qquad \mathbf{B} = -\frac{1}{i\omega}[\mathbf{e_0} \times \nabla_\perp]\nabla_\parallel \Phi, \qquad j_\parallel = -\frac{1}{i\mu_0\omega}\nabla_\perp^2 \nabla_\parallel \Phi, \tag{8}$$

where $\mathbf{e}_0 = \mathbf{B}_0/B_0$, $\nabla_\parallel = (\mathbf{e}_0 \cdot \nabla)$, and $\nabla_\perp = \nabla - \mathbf{e}_0 \nabla_\parallel$. The potential Φ is described by the 1-D wave equation (5). As follows from (8), horizontal components $\mathbf{E}_\perp$ and $\mathbf{B}_\perp$ and field-aligned current $j_\parallel$ of the incident wave are as follows:

$$E_1 = -(\partial_1 - \sin I \cos I \partial_3)\Phi, \quad E_2 = -\partial_2 \Phi, \tag{9}$$

$$B_1 = \frac{\sin^2 I}{i\omega}\partial_2\partial_3\Phi, \quad B_2 = -\frac{1}{i\omega}\left(\partial_1 - \sin I \cos I \partial_3\right)\partial_3\Phi, \tag{10}$$

$$j_\parallel = \frac{\sin I}{i\mu_0\omega}\left(\sin^{-2} I \partial_1^2 + \partial_2^2 + \cos^2 I \partial_3^2 - 2\cot I \partial_1 \partial_3\right)\partial_3 \Phi\,. \tag{11}$$

Various forms of incident wave transverse structures $\Phi(x^1, x^2)$ used in different modeling efforts are considered in the appendix. The scalar potential $\Phi(x)$ of the incident Alfvén wave beam in Model 1 is an asymmetric (odd) function of x in respect to the coordinate origin ($x = 0$), and in Model 2 the potential is a symmetric (even) function in respect to the axis $x = 0$. Here the transverse structure of an incident wave beam is mimicked by Model 1. The spatial distribution in the meridional plane perpendicular to $\mathbf{B}_0$ of the azimuthal magnetic component $B_2(x^1)$ in an incident wave is symmetric in respect to the beam center $x^1 = 0$ and has a maximum there. Also, we assume that the initial phase of the incident wave at the ionosphere-magnetosphere interface ($x^3 = z = z_*$) at $x^1 = 0$ ($x^1 = x - z_* \cot I$) is 0. The potential fitting these conditions can be chosen as follows:

$$\Phi(x', y', z') = \pm V_A b_0 x' \exp\left[-(x'/L_\perp)^2 + ik_{y'} y' \mp ik_A z'\right], \tag{12}$$

where $L_\perp$ is the beam characteristic scale along x' and upper/lower signs correspond to Southern Hemisphere/Northern Hemisphere. Here we introduce a local orthogonal coordinate system $\{x', y', z'\}$ with coordinate axis z' along the external magnetic field $\mathbf{B}_0$, the coordinate x' is measured in the meridional plane perpendicular to $\mathbf{B}_0$, and y' is the azimuthal coordinate (Figure 1). The introduced coordinates are related to the coordinates $\{x^1, x^2, x^3\}$ as follows: $x' = -x^1 \sin I$, $y' = x^2$, and $z' = -x^1 \cos I - x^3/\sin I$.

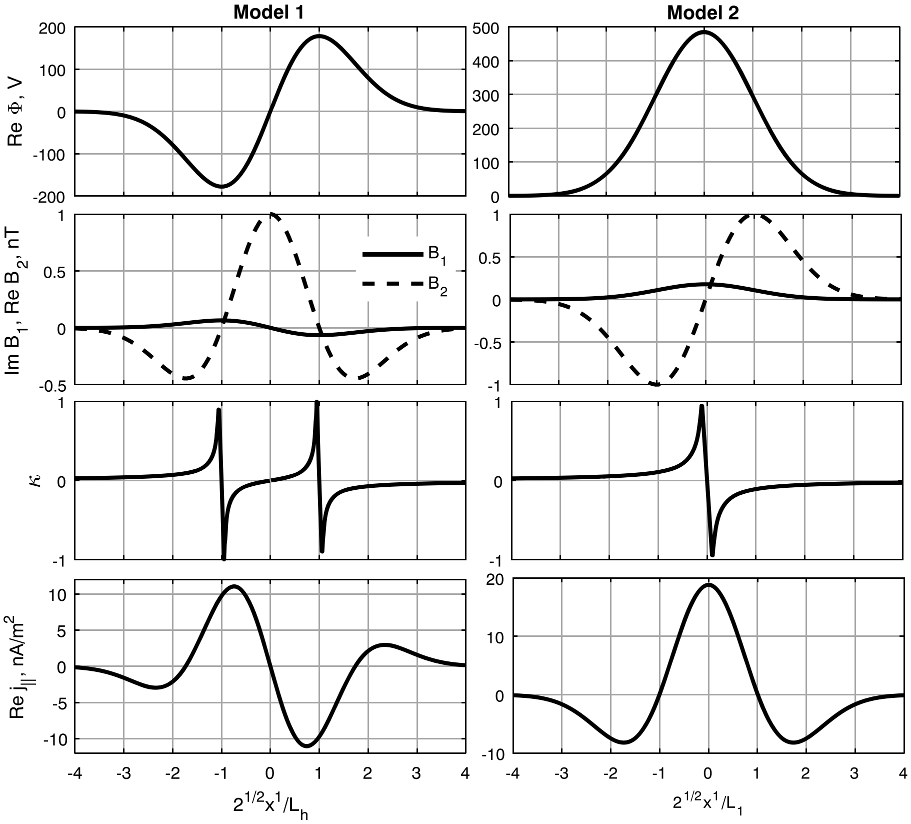

Figure 2. The dependence of the potential $\Phi(\bar{x})$, horizontal magnetic components $B_x(\bar{x})$, $B_y(\bar{x})$, ellipticity $\epsilon(\bar{x})$, and field-aligned current $j_{\|}(\bar{x})$ on the normalized distance $\bar{x} = \sqrt{2}x^1/L_h$ to the field line $x^1 = x - z_*\cot I = 0$ in the incident wave beam with $b_o = 1$ nT. Left-hand panels correspond to the Model 1 ($\Phi \propto \bar{x}\exp[-\bar{x}^2]$), and right-hand panels correspond to the Model 2 ($\Phi \propto \exp[-\bar{x}^2]$).

Then, as follows from (9)–(12), the latitudinal structure of the horizontal components $\mathbf{B}_\perp$, $\mathbf{E}_\perp$, and field-aligned current $j_{\|}$ in an incident wave at $z = z_*$ is as follows:

$$
\begin{aligned}
&B_1(x^1) = -ik_2 b_0 \sin^2 I x^1 \exp\left[-(x^1/L_h)^2 \pm ik_A x^1 \cos I\right],\\
&B_2(x^1) = b_0 \exp\left[-(x^1/L_h)^2 \pm ik_A x^1 \cos I\right]\left[1 - 2(x^1/L_h)^2\right],\\
&E_1(x^1) = -|\sin I| V_A B_2, E_2(x^1, x^2) = \frac{V_A}{|\sin I|} B_1,\\
&j_{\|}(x^1) = -\frac{b_0}{\mu_0}\frac{x^1}{L_h^2 \sin I}\exp\left[-(x^1/L_h)^2 \pm ik_A x^1 \cos I\right]\left[4\left(\frac{x^1}{L_h}\right)^2 - (k_2 L_h \sin I)^2 - 6\right],
\end{aligned}
\tag{13}
$$

where $L_h = L_\perp/|\sin I|$. In relationships (13) the factor $\exp(\mp ik_A x^3/\sin I + ik_2 x^2)$ has been omitted.

The dependence of the wave potential $\Phi(\bar{x})$, horizontal magnetic components $B_x(\bar{x})$, $B_y(\bar{x})$, ellipticity $\epsilon(\bar{x})$ (signed ratio between the small and large axis of the polarization ellipse), and field-aligned current $j_{\|}(\bar{x})$ on the normalized distance $\bar{x} = \sqrt{2}x^1/L_h$ to the field line of the beam center is shown in the left-hand panels of Figure 2. The potential $\Phi(\bar{x})$ is asymmetric in respect to the beam center $\bar{x} = 0$, so the amplitude $\Phi(\bar{x} = 0) = 0$. In the beam center $|\bar{x}| \ll 1$, the component $|B_x| \ll |B_y|$; that is, $\mathbf{B}$ is linearly polarized along the Y axis. In narrow intervals around $\bar{x} = \pm 1$, namely, $-(x^+, x^-)$ and (x^-, x^+), the components $|B_x/B_y| > 1$ and the main axis of the polarization ellipse are directed along the X axis. Here $x^\pm = \sqrt{1 + q^2} \pm q$, and $q = 2^{-3/2}k_2 L_h \sin^2 I$. In the central part of the beam, $|\bar{x}| < 1$, the rotation switches from left handed to right handed. At $\bar{x} = \pm 1$ the rotation changes sign again. This structure carries a pair of oppositely directed currents $j_{\|}$ in the central part of the beam, whereas another pair of weaker $j_{\|}$ flows at the edges of the beam (bottom panels in Figure 2).

The right-hand panels of Figure 2 show the spatial structure of the wave magnetic components, ellipticity, and field-aligned current in the case of symmetric spatial structure of the wave potential $\Phi(\bar{x})$ corresponding to the model (A5). According to (A6), in this case the structure of the wave azimuthal component $|B_y(\bar{x})|$ is antisymmetric in respect to the beam center $\bar{x} = 0$. Inside the beam the main axis of the polarization ellipse is predominantly oriented along the Y axis. Only in the proximity of the beam center $|\bar{x}| < \bar{x}_*$, where $\bar{x}_* = 2^{-1/2} k_2 L_h \sin^2 I$, the main axis becomes directed along the X axis. At the same time, the rotation sense also changes sign in the center of the beam $\bar{x} = 0$ from right handed to left handed. This wave structure carries $j_\parallel$ in the central part of the beam and closing currents of opposite polarity at the beam edges.

Both models predict the change of the ellipticity sign in the center of the beam. This feature was indeed observed in ST-5 multisatellite measurements (Balasis et al., 2016; Engebretson et al., 2008). However, the actual spatial structure of a typical Pc1 beam in the topside ionosphere has not been thoroughly examined yet. In this study, we only examine Model 1 with asymmetric $\Phi(x)$ wave potential structure, whereas Model 2 with asymmetric $\Phi(x)$ is left to future work. However, we do not expect great difference between these models in transmission/waveguide trapping features.

2.3. Model of the Medium

To reconstruct the altitude profile of the complex permittivity tensor elements (3), the IRI-2007 model (Bilitza & Reinisch, 2008) has been used. This empirical model provides height profiles of plasma parameters in the altitude range from $z = 60$ km up to the ionosphere-magnetosphere interface $z = 2,000$ km for any specified date and location. In addition, the Mass Spectrometer Incoherent Scatter model has been used to obtain the altitude profiles of temperatures and concentrations of various neutral particles. Using these parameters, the altitude profiles of the electron and ion collision frequencies $\nu_e(z)$ and $\nu_i(z)$ and consequently the tensor (3) components have been calculated using general formulas from Ginzburg (1970). Then, the profile of complex plasma conductivities $\sigma_P(z,\omega) = -i\omega\varepsilon_\perp(z,\omega)$, $\sigma_H(z,\omega) = -\omega g(z,\omega)$, $\sigma_\parallel(z,\omega) = -i\omega\varepsilon_\parallel(z,\omega)$, Alfvén velocity $V_A(z,\omega) = c\left(\mathrm{Re}\sqrt{\varepsilon_\perp(z)/\varepsilon_0}\right)^{-1}$ and the phase velocity in the field-aligned direction $V_{Ag} = \omega/k_\parallel$ (with account for the factor g that determines the gyrotropy of the plasma, or finite-frequency effect) have been calculated (Figure 3). V_{Ag} corresponds to the normal mode that reduces to the Alfvén normal mode well above the E layer, $V_{Ag} \simeq V_A$. The frequency dependence of the real parts of conductivities $\sigma_P(\omega)$, $\sigma_H(\omega)$ and the permittivity become negligible for low frequencies $\omega/\Omega \ll 1$, that is, when the wave frequency ω is much less than any ion gyrofrequency Ω. In this case the complex conductivities reduce to static Pedersen and Hall conductivities (0.5 Hz, left column of Figure 3). Upon increase of ω (4.0 Hz, right column of Figure 3), an additional maximum of the $\sigma_H(\omega,z)$ profile emerges at higher altitudes (~200 km). The negative sign of this maximum reduces the value of effective height-integrated Hall conductance $\Sigma_H(f)$ at high f.

The ground wave structure produced by magnetospheric Alfvén waves has been calculated for the conditions corresponding to the subauroral Halley (HAL) station: geographic coordinates −75.5°S, 333.4°E; corrected geomagnetic latitude $\Phi = -62.1°$ and longitude $\Lambda = 29.6°$, $I = -64.3°$, magnetic local time (MLT) noon is at 14:43 UT, and $L = 4.6$. The ground conductivity is assumed to be high, $\sigma_g = 10^{-3}$ S/m. The atmospheric conductivity is $\sigma_a = 1.1 \cdot 10^{-14}$ S/m at the ground surface. The vertical profile $\sigma_a(z)$ is modeled by an exponential function to match the conductivities predicted at $z = 80$ km by the IRI model. The results of the modeling may be qualitatively applied to any subauroral or midlatitude observation site.

2.4. Wave Modeling Parameters

To examine the modification of the wave beam structure, we have implemented the following approach: to decompose a magnetospheric wave structure $B(x)$ into spatial harmonics $B(k)$, multiply each of them by its scale-dependent transmission coefficient $T(k)$, and then compile all of them again to get a ground response, $B^{(g)}(x)$.

We suppose that the amplitude of the incident wave $b_0 = 1$ nT and the spectrum is flat $b_0(\omega) = \text{const}$. The azimuthal structure of the incident wave is characterized by a finite azimuthal wave scale $k_y = 1.7 \cdot 10^{-3}$ km^{-1} (corresponding to azimuthal wave number $m = 5$). Formally, the model considers a monochromatic wave as an incident signal. In reality, Pc1 waves have a finite duration (about 10–50 periods), and commonly, they are named as wave packets.

Examination of the spatial structure of Pc1 wave beams by the constellation of ST5 low-orbiting probes showed that the wave latitudinal scale is ~100 km (Engebretson et al., 2008). Simultaneous ground and satellite observations by Erlandson et al. (1996) estimated a latitudinal extent of the Pc1 source of ~120 km at ionospheric altitude. The Magsat satellite observations showed a source region of <100 km in the ionosphere (Iyemori & Hayashi, 1989). Thus, the modeling results for the incident wave scale $L_\perp = 10^2$ km are quite

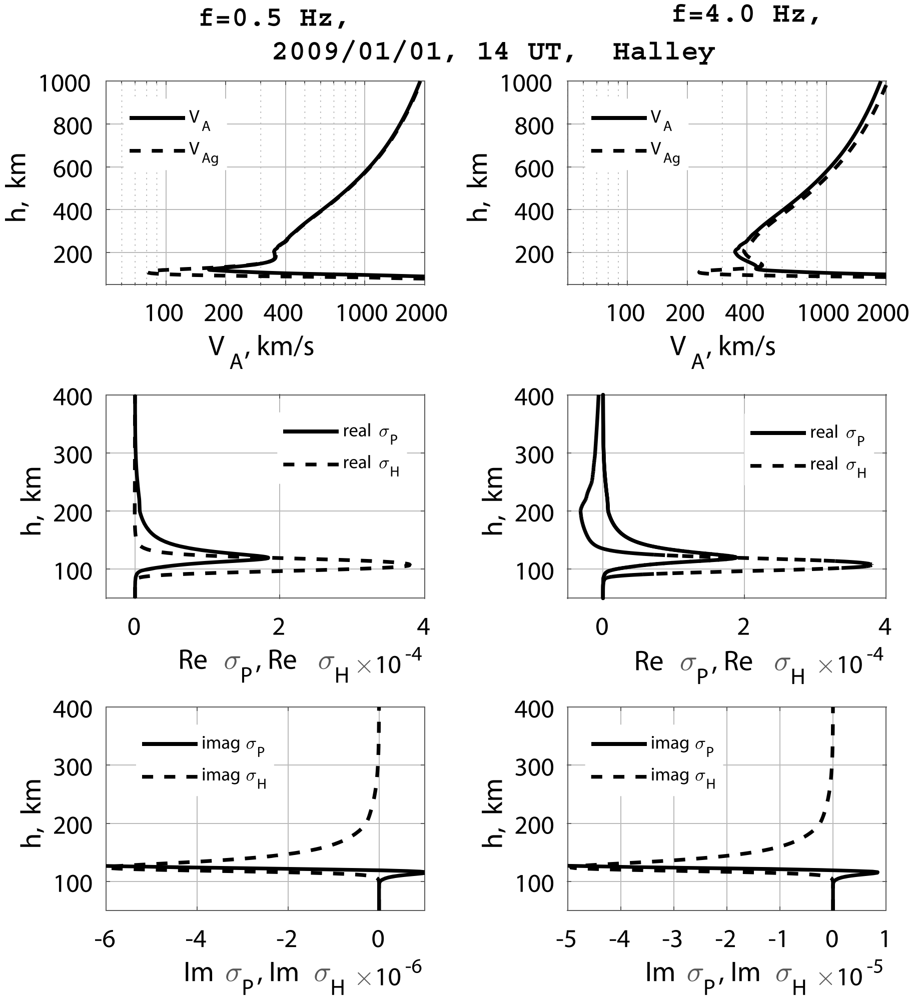

Figure 3. The altitude profiles for different frequencies: 0.5 Hz (left-hand panels) and 4.0 Hz (right-hand panels): (upper panels) Alfvén velocity $V_A(z)$ (solid lines) and field-aligned wave phase velocity $V_{Ag}(z)$ in [km/s] (dashed lines); (middle panels) real parts of complex plasma conductivities $\sigma_H(z)$, $\sigma_P(z)$ in [S/m], and (bottom panels) imaginary parts of complex plasma conductivities $\sigma_H(z)$, $\sigma_P(z)$ in [S/m]. The ionospheric conditions correspond to summer dayside ionosphere with $\Sigma_P = 5.6$ S, and $\Sigma_H = 9.3$ S.

relevant for the physics of Pc1 waves. This transverse scale $L_\perp$ corresponds to the horizontal scale $\sim$ 130 km in the E layer. An incident wave with such parameters will be nearly linearly polarized with dominating B_y component. This choice is supported by low Earth orbit satellite observations of EMIC waves (Kim et al., 2010).

3. Numerical Modeling Results

The ground wave structure produced by magnetospheric Alfvén waves will be considered next, using calculations consistent with the conditions given in the previous section. We apply the mathematical method of the impedance recomputation (nearly identical to the method of boundary condition transfer). The approach used here is similar to the technique of the reflection coefficient recomputation, used in Lehtinen and Inan (2008). The numerical solution of the system of wave equations is performed with the Runge-Kutta method for differential equation solutions. Calculations have been made for the year of solar minimum (2009). We compare results for local summer (1 January) for two extreme ionospheric conditions: daytime prenoon ionosphere (14 UT, MLT = 11:17 UT) and nighttime premidnight ionosphere (02 UT, MLT = 23:15 UT).

We will consider the latitudinal structure of the wave horizontal magnetic components on the ground for three characteristic frequencies: $f = 0.5$, 1.5, and 4.0 Hz, in the distance range $\pm 2 \cdot 10^3$ km from a source ($x = 0$). The direction $x \rightarrow +\infty$ corresponds to poleward (South Pole), and $x \rightarrow -\infty$ corresponds to equatorward

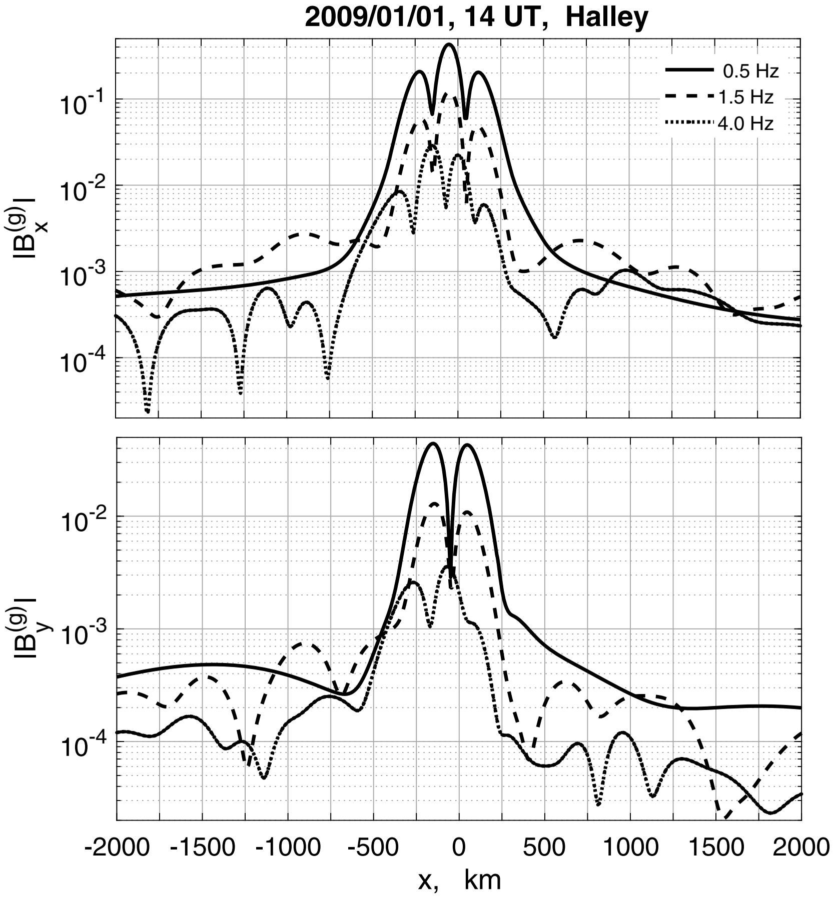

Figure 4. The latitudinal ground structure produced by Alfvén wave beam with scale 100 km and finite azimuthal scale ($k_y = 1.7 \cdot 10^{-3}$ km^{-1}), incident on the dayside (14 UT) summer (1 January) ionosphere for three different frequencies for magnitudes of $|B_x^{(g)}|$ component (upper panel) and $|B_y^{(g)}|$ component (bottom panel). $x > 0 (< 0)$ corresponds to the southward (northward) direction.

(North Pole) direction (Figure 1). After that, we will consider the spectra of horizontal magnetic components on the ground at various distances from the incidence point.

3.1. Daytime Ionosphere (14 UT)

The height-integrated Pedersen and Hall conductances are $\Sigma_P = 5.6$ S and $\Sigma_H = 9.3$ S, corresponding to typical daytime midlatitude conditions. On the ground the coordinates match the conditions $x^3 = z = 0$ and $x^1 = x$. Therefore, here and further instead of x^1 axis we use x axis.

3.1.1. Spatial Structure

Figure 4 shows the distribution of amplitudes of horizontal magnetic components $|B_x^{(g)}(x)|$ (upper panel) and $|B_y^{(g)}(x)|$ (bottom panel). The semiwidth of $|B_x^{(g)}(x)|$ on the ground surface (measured as the distance between the major and minor maxima), ~170 km, is wider by ~40 km as compared with that of the incident wave beam in the E layer of the ionosphere (~130 km). The difference between beam widths follows from the difference of their spatial spectra. The ratio of spatial harmonics amplitudes on the ground and in the ionosphere is $\propto \exp(-|k_1|h)$. As follows, on the ground the spatial spectrum is enriched with the harmonics with long spatial scales as compared with that in the incident beam. As a result, the beam on the ground is wider than the incident beam.

Modeling shows that the contribution of the electric mode into the ground wave structure is weak and within the considered distance range ≤2,000 km can be neglected. The ground response is due practically totally to the magnetic mode. The ground magnetic response is nearly in phase within a distance ~300 km from a source center. At these distances the magnetostatic field generated in the atmosphere by the Alfvén wave-induced ionospheric Hall currents dominates.

The latitudinal structure of $|B_x^{(g)}(x)|$ demonstrates an equatorward shift Δx of the amplitude peak in respect to the footprint of the incident wave beam maximum ($x = 0$; Figure 4). This shift approximately coincides with the vertical footprint of the maximum of ionospheric Hall conductivity, $\Delta x \simeq h|\cot I|$, where h is the effective height of the Hall current. Using the distributions of Hall conductivity $\sigma_H(z, f$; Figure 3), we get h values for the frequencies analyzed: $h \simeq 110$ km for $f = 0.5$ and 1.5 Hz and $h \simeq 300$ km for $f = 4$ Hz. As the effective altitude of the conductive layer $h(f)$ grows with frequency, $\Delta x(f)$ increases with frequency, as well: $\Delta x \simeq 50$ km for $f = 0.5$ and 1.5 Hz and $\Delta x \simeq 150$ km for $f = 4$ Hz.

Within the main maximum, narrow amplitude dropouts of $|B_x^{(g)}(x)|$ can be seen at $x \simeq -150$ km and 50 km for $f = 0.5$ and 1.5 Hz, and of $|B_y^{(g)}(x)|$ at $x \simeq -50$ km for $f = 0.5$ and 1.5 Hz. These dropouts correspond to magnetic field nodes in the spatial structure of the components of the incident beam (see Figure 2, second panels from the top).

The amplitude of the N-S component $|B_x^{(g)}|$ is larger by nearly an order of magnitude than the amplitude of the azimuthal component $|B_y^{(g)}|$ at all distances for $f = 0.5$ Hz. The latitudinal dependence of $B_x^{(g)}(x)$ and $B_y^{(g)}(x)$ duplicates qualitatively (with account for a shift by Δx, rotation by $\pi/2$, and some widening) the spatial distributions of magnetic components in the incident Alfvén beam within the beam scale, $|x| \leq 300$ km.

The wave spreading along the ionosphere is commonly imagined as a leakage of wave energy from an incidence region by propagating IFW modes. If so, the wave structure should appear to have a gradually decaying amplitude and growing phase with distance. The pattern shown in Figure 4 demonstrates an inhomogeneous decay of wave amplitude; that is, the local decay rate varies with distance. The largest decay rate is observed near the edges of the ground image of the incident beam, for example, at $f = 0.5$ Hz, $|B_x^{(g)}(x = 100\text{km})/B_x^{(g)}(x = 300\text{km})| \simeq 12$, which is ~10 dB/100 km, whereas $|B_x^{(g)}(x = 370\text{km})/B_x^{(g)}(x = 720\text{km})| \simeq 7$, which is ~5 dB/100 km. The modeled decay rate cannot be directly compared with the observed rate, because the actual value of the beam azimuthal scale is not known. Nonetheless, any other choice of k_y will not qualitatively modify the spatial structure on the ground.

At larger distances $|x| \geq 400$ km, the contribution of the quasi-static magnetic field from Hall currents in the incidence region to the ground magnetic response decreases rapidly with distance. Indeed, in the ultralow frequency range all magnetic modes are evanescent $\propto \exp(-n\pi x/h)$ and decay rapidly away from a source. For example, the nth mode of the atmospheric waveguide decreases at distance 400 km by a factor of $\sim 3 \cdot 10^{-6}$, and its ground magnetic effect is small as compared with the effect of IFW modes. The waveguide critical frequency is estimated to be $f_* \approx 0.3$ Hz. Therefore, for $f = 0.5$ Hz there is only one IFW mode in the ionospheric waveguide, which amplitude decays monotonically with distance (Figure 4), but at distances >300 km the contribution of IFW mode becomes prevailing. The complicated spatial pattern at higher frequencies, that is, at 1.5 and 4.0 Hz, occurs because of interference between several waveguide modes.

The latitudinal wave structure is almost symmetric at $f = 0.5$ Hz. However, at higher $f \geq 1.5$ Hz, away from the incidence region, the dependence of the field amplitude on distance is nonmonotonic, oscillatory, and asymmetric in respect to the northward and southward directions. Locations of extremes in latitudinal distribution of amplitudes are frequency dependent and nonsymmetric relative to the beam incidence point.

The amplitude of the $B_y^{(g)}$ component is in general several times lower than that of $B_x^{(g)}$ component. Only in narrow ranges of distances near minima of $|B_x^{(g)}(x)|$ can the component $|B_y^{(g)}|$ exceed $|B_x^{(g)}|$. For example, at $f = 1.5$ Hz the amplitude of $B_y^{(g)}$ becomes larger than that of $B_x^{(g)}$ inside two narrow intervals (−150,−4140) and (40,54) km. These very narrow dropouts of $|B_x^{(g)}(x)|$ would be hard to observe on the ground with a typical array of magnetometers separated by at least several hundred kilometers.

3.1.2. Spectra at Various Distances

The ground spectra at various distances from the incidence point ($x = 0$) up to $x = 1,000$ km are presented in Figure 5. In a realistic situation, the spectrum of an incident EMIC wave $b_0(f)$ would be superposed onto the presented spectra, $|B_x^{(g)}(f)|$ and $|B_y^{(g)}(f)|$.

As follows from the comparison of main ground peak amplitudes with the amplitude of the incident wave (1 nT), the ground response to incident wave tends to decrease with frequency. The values of $|B_x^{(g)}|$ in the main peaks, as one can see from Figure 4, are ~0.4 nT at $f = 0.5$ Hz, ~ 0.1 nT at $f = 1.5$ Hz, and ~ 0.03 nT at $f = 4.0$ Hz. Decrease of the transmission efficiency with frequency is probably caused by several factors: (a) The ratio of absolute values of complex Hall and Pedersen conductances $|\Sigma_H(f)/\Sigma_P(f)|$ decreases several times

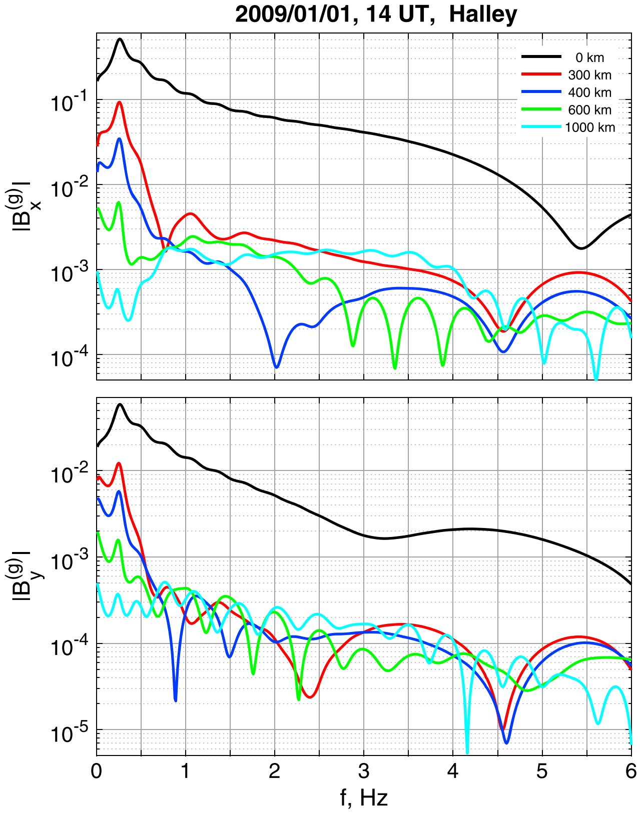

Figure 5. The spectra of ground response $B_x^{(g)}(f)$ (upper panel) and $B_y^{(g)}(f)$ (bottom panel) to Alfvén wave beam with white spectrum and with $k_y = 1.7 \cdot 10^{-3}$ km^{-1} incident on the dayside (14 UT) summer ionosphere at various distances (shown in legend) from the incidence point.

upon frequency growth from $f = 0.5$ to 6 Hz; (b) The Alfvén wave electric field E_x and Hall current $j_y = \sigma_H E_x$ oscillate with altitude. The wavelength of these oscillations along a field line is the Alfvén wavelength, and it depends on frequency as $\lambda_A \propto 1/f$. The resulting ground magnetic field from such oscillatory Hall current decreases as $\propto 1/f$; (c) Joule dissipation in the ionosphere enhances at the IAR resonant frequencies and in general grows with frequency. Due to the factors mentioned above, the amplitude of a transmitted signal under the incident beam should decrease with frequency even faster than $1/f$. This conclusion roughly agrees with the numerical solution for $x = 0$ at the dayside (Figure 5) at frequencies exceeding the IAR fundamental frequency $f_1 \approx 0.25$ Hz. The amplitude of ground response $B_x^{(g)}$ at $x = 0$ km decreases by almost 2 orders of magnitude from ~0.3 nT at $f = 0.5$ Hz to $\sim 4 \cdot 10^{-3}$ nT at $f = 6$ Hz. At the same time, the amplitude of $B_x^{(g)}$ far from the beam axis is controlled by the waveguide modes and the decrease of amplitude with frequency is not so steep. However, at $x > 300$ km the amplitude decrease with frequency $|B_x^{(g)}(f)|$ becomes nonmonotonic owing to interference of waveguide modes.

The spectral peak at the fundamental IAR eigenfrequency ~ 0.25 Hz is highlighted in both $|B_x^{(g)}(f)|$ and $|B_y^{(g)}(f)|$ spectra at all the distances from the incident beam axis. Thus, the IAR makes a "transmission spectral window" in the band around its fundamental eigenfrequency. The second IAR harmonic with $f_2 \simeq 0.5$ Hz is only weakly revealed at distances $|x| \leq 400$ km as a change of the spectral amplitude decay rate. However, a clear maximum at the second IAR harmonic can be seen at $x = 600$ km in $|B_x^{(g)}(f)|$ and at $x \geq 600$ km in $|B_y^{(g)}(f)|$. Higher IAR harmonics practically do not reveal themselves on the background of fast decay of amplitude with frequency. Thus, for a realistic localized beam the transmission window can be formed at the IAR fundamental eigenfrequency only, but not at higher IAR harmonics.

At longer distances ($x > 400$ km) additional multiple spectral peaks associated with IFW modes become evident (Figure 5). The frequencies of these peaks do not coincide with resonant IAR frequencies. Thus, at large distances from an incidence point the transmission windows associated with the IFW modes compete with the IAR-related "windows."

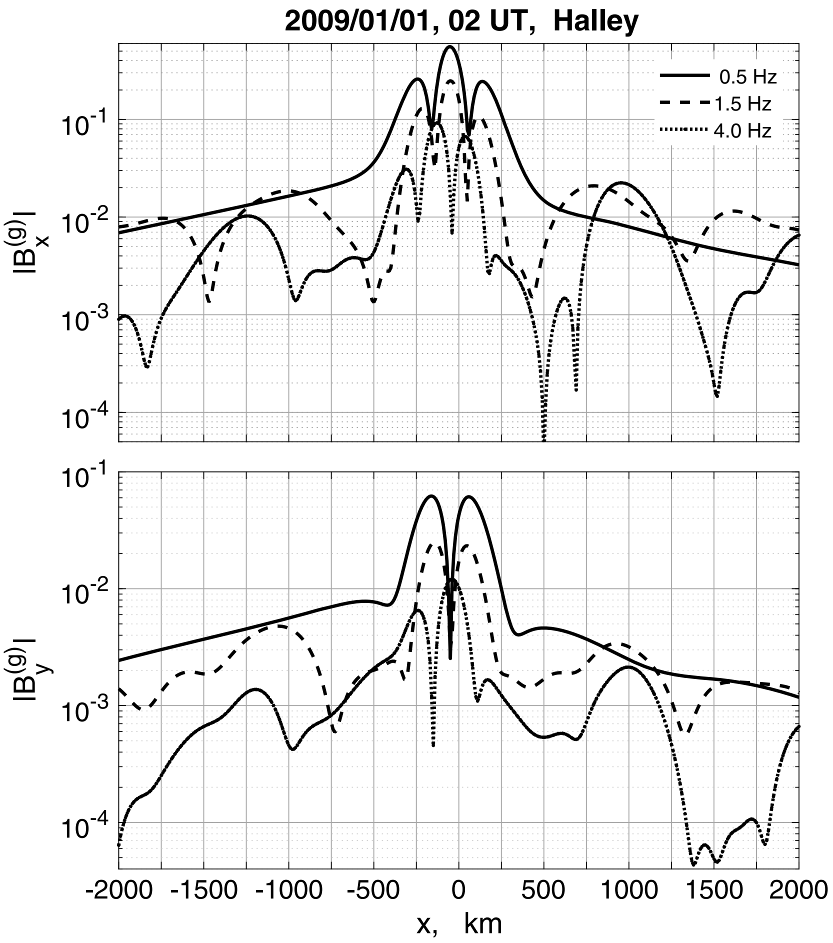

Figure 6. The latitudinal structure of amplitudes of horizontal magnetic components $|B_x^{(g)}(x)|$ (upper panel) and $|B_y^{(g)}(x)|$ (bottom panel) produced by Alfvén wave beam with $k_y = 1.7 \cdot 10^{-3}$ km^{-1} incident on the nightside (02 UT) summer ionosphere for three different frequencies.

3.2. Nighttime Ionosphere (02 UT)

The static height-integrated Pedersen and Hall conductances for the nightside case are $\Sigma_P = 2.1$ S and $\Sigma_H = 3.3$ S.

3.2.1. Spatial Structure

Beneath the incident beam, at $|x| \leq 300$ km, the ground structure duplicates the $\pi/2$-rotated structure of the incident beam and it is shifted equatorward as a whole from the wave incidence point by $\Delta x \simeq -50$ km for $f = 0.5 - 1.5$ Hz and $\Delta x \simeq -150$ km for $f = 4.0$ Hz, similar to the dayside case (Figure 6).

During the nighttime period (Figure 6) the attenuation in the ionosphere at $f = 0.5$ Hz is nearly the same as during the daytime: the main peak ground amplitude is ~0.6 nT. Comparison of Figures 4 and 6 shows that at nighttime for distances $|x| \leq 600$ km the spatial decay of the amplitude of the horizontal magnetic components is not as strong as during the daytime. For example, at $f = 0.5$ Hz the ratio $|B_x^{(g)}(x = 100\text{km})/B_x^{(g)}(x = 300\text{km})|$ is ~12, whereas during the nighttime it is ~3. In other words, during nighttime, at $|x| < 600$ km $|B_x^{(g)}(x)|$ decreases by ~1 dB/100 km, while at daytime the decrease is faster ~10 dB/100 km. At distances $|x| \geq 600$ km the nighttime and daytime decay rates are nearly the same, ~1 dB/100 km.

At higher frequencies the decay of amplitude away from the incidence region is nonmonotonic due to interference between different IFW modes. At $f = 1.5$ Hz nighttime local minima (~$1.5 \cdot 10^{-3}$ nT and ~$3.5 \cdot 10^{-3}$ nT) and local maxima (~$2 \cdot 10^{-2}$ nT) are formed at $x \simeq 435$, 1,350, and 800 km from the source, respectively, with the spatial scale ~10^3 km. This oscillatory structure is produced by the interference of two waveguide modes with the difference of wave numbers $\Delta k \simeq 6 \cdot 10^{-3}$ 1/km. For $f = 4.0$ Hz the spatial oscillatory structure with

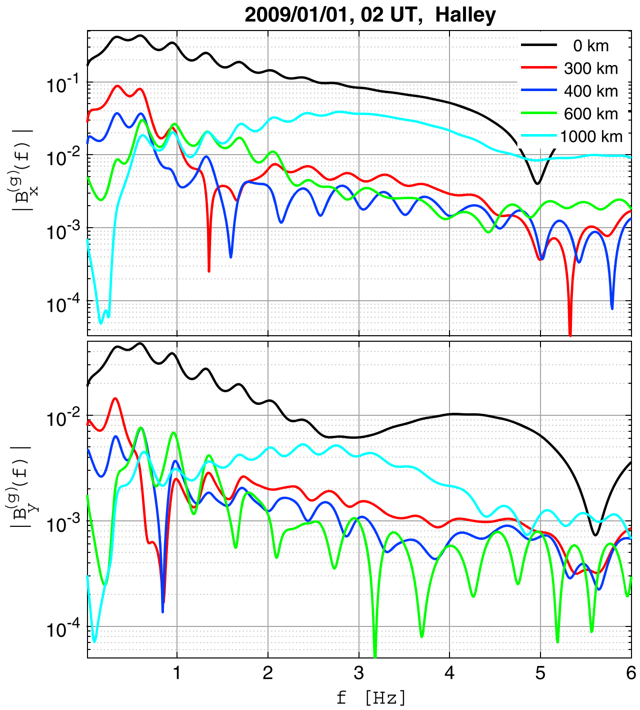

Figure 7. The spectra of the amplitude of ground magnetic response $B_x^{(g)}(f)$ (upper panel) and $B_y^{(g)}(f)$ (bottom panel) to Alfvén wave beam with white spectrum and $k_y = 1.7 \cdot 10^{-3}$ km^{-1} impinging on the nightside (02 UT) summer ionosphere at various distances from the incidence point (shown in legend).

two spatial scales 200 and 600 km is formed by the interference of several modes with different horizontal scales. As a result, the distance between minima and maxima of spatial structure is not constant.

3.3. Spectra at Various Distances

The nighttime ground spectra at various distances from the beam axis are presented in Figure 7. At all distances spectral peaks in $|B_x(f)|$ and $|B_y(f)|$ can be seen at 0.34, 0.6, 0.95, 1.32, and 1.7 Hz. The frequencies of these spectral peaks practically do not depend on distance, and they are associated with the IAR excitation. However, in most regions the expected spectral maxima associated with IAR harmonics are hardly evident, because they are masked by interference extremes of IFW modes.

At higher frequencies, $f > 2$ Hz, a multiband spectral structure of $B_x^{(g)}(f)$ and $B_y^{(g)}(f)$ components with many small spectral peaks with frequency scale $\Delta f \simeq 0.4$ Hz can be seen (Figure 7). Their frequencies vary with distance, and they are associated with the IFW modes.

4. Discussion

One of the key problems of magnetospheric physics is how well do ground Pc1 observations characterize EMIC wave activity in the magnetosphere? How significantly can the transmission/reflection properties of the ionosphere modify the growth and spectral content of Pc1 waves? Quantitative answers to these questions may help to parameterize the contribution of EMIC wave activity into radiation belt models using ground-based data (Drozdov et al., 2017). In an attempt to answer these questions, we have presented a numerical model based on the solution of full-wave equations for coupled MHD modes in a realistic IRI ionosphere. This model has been applied to the interpretation of daily variations of the ground response at middle latitude to magnetospheric EMIC waves.

The power and occurrence rate of Pc1 waves on the ground are determined by three processes: generation in the near-equatorial plane of the magnetosphere, field-aligned propagation from the top of the field line to the upper ionosphere, and transmission through the ionosphere to the ground. The presented model describes the third process only, so it cannot be directly applied to interpret all features of the ground

Pc1 activity. Nonetheless, the model may be used to comprehend some fine features of Pc1 observations. Here we have considered only the spatial and spectral amplitude structures. Polarization properties will be considered elsewhere.

The transmission of Pc1 waves through a realistic ionosphere is a complicated process comprising mutual interaction of various MHD and electromagnetic modes. The frequency dependence of the efficiency of Alfvén wave transmission through the ionosphere is determined by eigenfrequencies of the IAR and IFW modes. IAR resonant frequencies do not depend on the wave scale, whereas IFW frequencies are strongly scale dependent. Waveguide modes in the upper ionosphere have a cutoff frequency, so they do not exist for large scales and low frequencies. Though the scale-dependent coupling of the IAR and IFW modes dictates the necessity to consider the ionospheric transmission properties for different wave scales, here a typical scale of 100 km according to low Earth orbit satellite observations has been chosen. A comparison of transmission properties for different transverse scales will be given elsewhere.

Modeling has indicated that the electric mode in the atmospheric waveguide does not produce a noticeable contribution. The amplitude of the magnetic component, associated with this mode, is much weaker than that of the magnetic H-mode at all distances under consideration. Therefore, the conception based on the electric mode can hardly be applied to interpret pulsations of the atmospheric vertical electric field in the ultralow frequency band (Chetaiev et al., 1975).

Numerical modeling shows that the latitudinal structure of magnetic components on the ground duplicates qualitatively the spatial structure of magnetic components within the incident Alfvén beam (with account for some latitudinal shift Δx, $\pi/2$ rotation, and spatial widening—on the ground the amplitude maximum has an increased semiwidth by ~60 km as compared with that in the incident beam). Thus, prominent features of the Pc1 spatial structure, such as the reversal of polarization and pivot of the ellipse orientation, predicted by numerical models (Fujita & Tamao, 1988; Woodroffe & Lysak, 2012), are, in fact, caused by the assumed structure of an incident wave but not by effects of propagation along the ionosphere. Both in the incident beam and in its ground response, the polarization rotation changes in the beam center (region of maximal amplitude). Also, the rotation changes near the amplitude minima of $|B_x(x)|$, coinciding with maxima of $|B_y(x)|$. The spatial structures of an incident wave beam used in different models are compared in the appendix. The existing satellite and ground observations (Pilipenko & Heilig, 2016) do not provide, so far, information about wave spatial structure with sufficiently high spatial resolution to make a justified choice between these models.

The modeling has shown that the wave amplitude decays rapidly with distance from a source at the edges of the beam. Farther away, the spatial decay rate becomes smaller but very inhomogeneous. Upon the transition from a quasi-static zone to a wave zone, at $|x| > 300$ km, the wave structure on the ground is controlled by the IFW mode interference. As a result of this interference, the wave amplitude latitudinal distribution becomes nonmonotonic.

The results of numerical modeling correspond to some observed properties of Pc1 waves recorded at ground magnetometer arrays. The amplitude distribution of Pc1 waves along multistation arrays showed that the propagation from a source was not isotropic but tends to align with geomagnetic latitude (Hayashi et al., 1981). The spatial gradient of amplitude near the source region was found to be large, ~10 dB/100 km. Antarctic search coil magnetometer arrays along a magnetic meridian, spanning nearly 3,000 km, showed poleward propagation of the Pc 1 waves in the ionospheric waveguide (Kim et al., 2010). A tendency was noticed for the attenuation factor (8–20 dB/1,000 km) to increase with increasing frequency. At the same time, the stations located far from a source showed no clear tendency of spectral power attenuation. These features are in agreement with our modeling results.

Observations at an array of induction magnetometers in Japan showed that while Pc1 pulsations at high latitudes were most frequently observed during the daytime, at low latitudes the occurrence maximum was always in the nighttime (Kuwashima et al., 1981; Nomura et al., 2011). This observational fact indicates that the attenuation of Pc1 waves upon propagation via the ionospheric waveguide toward lower latitudes is weaker during night hours, in accordance with the modeling results.

A multiband spectral structure can be formed not only in the magnetosphere due to heavy ion effects, for example, Lee et al. (2008), but upon wave propagation through the ionosphere. This possibility was suggested in Mursula et al. (2000) and Prikner et al. (2001, 2004), who interpreted Pc1 spectral peaks as high order ($n = 3$–4) IAR harmonics. Our calculations have shown that for a realistic localized beam a significant transmission window can be formed at the IAR fundamental eigenfrequency only but not at higher IAR harmonics. A possible verification of this prediction could be done by analyzing the dynamic spectra of nighttime Pc1 events. The frequency of Pc1 emissions should demonstrate a tendency to overlap with the lowest frequency of a simultaneous IAR spectral structure.

A multiband spectral structure can be formed also upon ducted wave propagation along the ionosphere. The occurrence of multiple spectral band structures was noticed by Kim et al. (2010) while analyzing Pc1 observations along a very extended array. As another example, we mention the examination of a long-lasting Pc1 event detected at an extensive array (11 stations) in Mann et al. (2014). The emission with largest power near the source region was band limited around 0.7 Hz, while far away from it the wave power was significantly decreased and split into two bands, around 0.6 and 1.2 Hz. We suppose that the occurrence of a higher-frequency spectral band at $\sim$1.2 Hz is due to IFW modes. However, to reveal the effect of spectral modification upon ionospheric propagation, a comparison of spectrograms from multiple sites in the Pc1 band is necessary, and such study is still awaiting.

Besides the spectral peak associated with IAR and IFW modes, additional wide spectral peaks with semiwidth of about several hertz, and bounded by dips of magnetic field spectra, can be seen (Figures 5 and 7). Ermakova et al. (2007) suggested that such a wide maximum is associated with the resonator in the lower ionosphere (sub-IAR), between the E layer and the bottom of the F layer. On the other hand, Fedorov, Mazur, Pilipenko, and Engebretson (2016) supposed that these spectral maxima are possibly related to synchronization of Alfvén and magnetosonic modes upon wave transmission through the ionosphere. Thus, the physical mechanism of the wide spectral maximum has not been firmly established and needs more detailed consideration.

In general, the presented model of a localized wave beam has confirmed basic results of consideration in Fedorov, Mazur, Pilipenko, and Engebretson (2016) based on the plane wave approximation. Both the “plane wave” and “beam” models showed the formation of transmission windows at the IAR eigenfrequencies, in accord with known results. However, the beam model has demonstrated that only the first 1–2 IAR harmonics appear in ground spectra, whereas spectral features at higher IAR harmonics are smoothed away. Both models predict the occurrence at large distances of spectral signatures related to waveguide modes. The plane wave modeling found a wide spectral enhancement in a frequency domain slightly above the IAR harmonics. Though evidence of similar structure can be seen in the beam modeling as well, a detailed consideration of this effect will be given elsewhere.

5. Conclusion

Pc1 wave transmission through the ionosphere is a complicated process where different wave modes in the ionosphere and atmosphere are coupled and the coupling rate depends on media parameters (anisotropy of conductivity and magnetic field inclination) and wave characteristics (spatial scale and frequency). The occurrence of the IAR and fast-mode waveguide, which can trap electromagnetic wave energy in the range from fractions of a hertz to a few tens of hertz, ensures the complicated dependence of the ionospheric transmission properties on frequency, wave scale, and distance from a source. The model presented here is based on the numerical solution of full-wave equations for coupled Alfvén and fast magnetosonic modes in a realistic IRI-derived ionosphere, excited by a latitudinally localized beam of magnetospheric Alfvén wave. Beneath the beam, the ground structure duplicates the structure of the incident magnetospheric wave but with account of some peculiarities: $\pi/2$ rotation, latitudinal shift, and structure widening. The model predicts that the upper part of the Pc1 spectrum ($f > 1$ Hz) is to be attenuated upon wave transmission through the ionosphere to the ground, especially during the daytime. A local decay of wave amplitude on the ground varies strongly with distance. The latitudinal structure of the ground response to an incident Alfvén wave beam at $f > 1$ Hz can be nonmonotonic owing to the interference of the IAR and IFW modes. The transmission of Alfvén waves has a dependence on frequency with a narrow transmission window at the fundamental IAR eigenfrequency. Additional spectral windows are formed at large distances from the incidence location owing to ionospheric waveguide modes.

Appendix A: Incident Wave Structures in Various Models

Prominent features of the Pc1 spatial structure, such as reversal of polarization, pivot of the ellipse orientation, predicted by numerical models (Fujita & Tamao, 1988; Woodroffe & Lysak, 2012), are, in fact, produced by the assumed structure of an incident wave but not by propagation effect along the ionosphere. Therefore, a comparison of basic assumptions of various models is important.

A1. Model 1

The scalar potential of the incident Alfvén wave in Fujita and Tamao (1988) was set as an asymmetric function:

$$\Phi(\rho,\phi) \propto (\rho/\rho_0)^{|m|}\exp[-(\rho/\rho_0)^2 + im\phi], \tag{A1}$$

where $\{\rho,\varphi,z\}$ is a cylindrical coordinate system and ρ_0 is the scale of radial localization of the incident wave. The case $m = -1$ was chosen. The structure (A1) is qualitatively similar to ours (12).

In any wave structure localized in the radial direction and propagating in the azimuthal direction, the polarization sense ϵ, which depends on the slope $d\Phi/d\rho$, must change sign at some ρ for the non-monotonic structure as (A1). Thus, the change of polarization sense across a certain demarcation line is related not to the propagation effect but to the structure of incident wave. The change of the major axis of the polarization ellipse direction at larger distances from an incident region is related to different decay rates of $B_x(\rho)$ and $B_y(\rho)$ components in the incident wave structure.

For the antisymmetric potential (12), the spatial harmonics of the azimuthal magnetic component can be found from (13):

$$B_y(k_1) = 2^{-3/2}L_h b_0(\omega)(k_1 \mp k_A \cos I)^2 L_h^2 \exp\left\{-(k_1 \mp k_A \cos I)^2 L_h^2/4\right\}. \tag{A2}$$

The ground structure is the result of convolution of the spatial spectrum (A2) with the transmission coefficient $T(k_1)$.

A2. Model 2

In modeling the transverse structure of an incident Alfvén beam Woodroffe and Lysak (2012) assumed the symmetric form of the potential

$$\Phi(\rho,\varphi) \propto \Phi_0 \exp\left[-\left(\frac{\varphi-\varphi_0}{\Delta\varphi}\right)^2 - \left(\frac{\rho-\rho_0}{\Delta\rho}\right)^2\right]. \tag{A3}$$

In an oblique coordinate system the potential (A3) has the following form. Let us consider a localized wave structure, so $\Delta\rho/\rho_0 \ll 1$ and $\Delta\varphi \ll 1$. Then approximately $x^1 \simeq -(\rho-\rho_0)/\sin I$, and $x^2 \simeq \rho_0(\varphi-\varphi_0)$. As a result, the potential (A3) can be written as follows:

$$\Phi(x^1,x^2) \propto \exp\left[-(x^1/L_1)^2 - (x^2/L_2)^2 \pm ik_A(x^1\cos I + x^3/\sin I)\right], \tag{A4}$$

where $L_1 = \Delta\varrho$, $L_2 = \rho_0\Delta\varphi$ are scales of a disturbance along ϱ and φ, and upper/lower signs correspond to Southern Hemisphere/Northern Hemisphere.

Here we consider only the Fourier harmonic with the azimuthal wave number k_2. The decomposition of (A4) into spatial harmonics $\propto \exp(ik_2x^2)$ provides

$$\Phi(x^1,k_2) = 2^{-1/2}L_1V_A|\sin I|b_0\exp\left[-(x^1/L_1)^2 \pm ik_A(x^1\cos I + x^3/\sin I) + 1/2\right]. \tag{A5}$$

Substitution of (A5) into ((9)–(11)) gives the following structures of the horizontal magnetic components and field-aligned current transported by incident Alfvén wave:

$$\begin{aligned} B_1 &= ik_2\frac{|\sin I|}{V_A}\Phi, \qquad E_2 = V_A|\sin I|B_1,\\ B_2 &= \frac{2x^1}{V_AL_1^2|\sin I|}\Phi, \qquad E_1 = -V_A|\sin I|B_2,\\ j_\parallel &= \mp\frac{2}{\mu_0V_AL_1^2\sin^2 I}\left[2\left(\frac{x^1}{L_1}\right)^2 - 1 - \frac{k_2^2L_1^2\sin^2 I}{2}\right]. \end{aligned} \tag{A6}$$

This structure shown in the right-hand panels in Figure 2 carries the field-aligned current in the central part of the beam and closing currents of opposite polarity at beam edges.

Acknowledgments

This research is supported by a grant 18-05-00108 (VAP) from the Russian Fund for Basic Research, state contract with the Institute of Physics of the Earth (ENF), and grants PLR-1341493 (MJE) and PLR-1543364 (MDH) from the U.S. National Science Foundation. The numerical code incorporates the IRI model (iri.gsfc.nasa.gov) and the MSIS model (ccmc.gsfc.nasa.gov/modelweb/atmos/msise.html). Calculations with the elaborated code for any geophysical conditions may be requested from the authors. We appreciate thorough reading and helpful comments of both reviewers.

References

Alperovich, L. S., & Fedorov, E. N. (1992). On hydromagnetic wave beams propagation through the ionosphere. *Annales Geophysicae*, *10*, 647–654.

Alperovich, L. S., & Fedorov, E. N. (2007). *Hydromagnetic waves in the magnetosphere and the ionosphere, Series: Astrophysics and Space Science Library* (Vol. 353, pp. XXIV, 418). Netherlands: Springer.

Anderson, B. J., Erlandson, R. E., & Zanetti, L. J. (1992). A statistical study of Pc 1-2 magnetic pulsations in the equatorial magnetosphere: 1. Equatorial occurrence distributions. *Journal of Geophysical Research*, *97*, 3075–3088.

Arnoldy, R. L., Engebretson, M. J., Denton, R. E., Posch, J. L., Lessard, M. R., Maynard, N. C., et al. (2005). Pc 1 waves and associated unstable distributions of magnetospheric protons observed during a solar wind pressure pulse. *Journal of Geophysical Research*, *110*, A07229. https://doi.org/10.1029/2005JA011041

Balasis, G., Papadimitriou, C., Zesta, E., & Pilipenko, V. (2016). Monitoring ULF waves from low Earth orbit satellites. In *"Waves, particles, and storms in Geospace"* (pp. 148–169). Oxford, UK: Oxford University Press.

Belyaev, P. P., Polyakov, S. V., Rapoport, V. O., & Trakhtengertz, V. Y. (1990). The ionospheric Alfvén resonator. *Journal of Atmospheric and Solar-Terrestrial Physics*, *52*, 781–787.

Bilitza, D., & Reinisch, B. (2008). International Reference Ionosphere 2007: Improvements and new parameters. *Advances in Space Research*, *42*, 599–609.

Chetaiev, D. N., Fedorov, E. N., Krylov, S. M., Lependin, V. P., Morghounov, V. A., Troitskaya, V. A., & Zybin, K. Y. u. (1975). On the vertical electric component of the geomagnetic pulsation field. *Planetary and Space Science*, *23*, 311–314.

Daglis, I. A., Thorne, R. M., Baumjohann, W., & Orsini, S. (1999). The terrestrial ring current: Origin, formation, and decay. *Reviews of Geophysics*, *37*, 407–438.

Demekhov, A. G. (2012). Coupling at the atmosphere-ionosphere-magnetosphere interface and resonant phenomena in the ULF range. *Space Science Reviews*, *168*, 595–609.

Demekhov, A. G., Belyaev, P. P., Isaev, S. V., Manninen, J., Turunen, T., & Kangas, J. (2000). Modeling the diurnal evolution of the resonance spectral structure of the atmospheric noise background in the Pc 1 frequency range. *Journal of Atmospheric and Solar-Terrestrial Physics*, *62*, 257–265.

Drozdov, A. Y., Shprits, Y. Y., Usanova, M. E., Aseev, N. A., Kellerman, A. C., & Zhu, H. (2017). EMIC wave parameterization in the long-term VERB code simulation. *Journal of Geophysical Research: Space Physics*, *122*, 8488–8501. https://doi.org/10.1002/2017JA024389

Engebretson, M. J., Posch, J. L., Westerman, A. M., Otto, N. J., Slavin, J. A., Le, G., et al. (2008). Temporal and spatial characteristics of Pc1 waves observed by ST5. *Journal of Geophysical Research*, *113*, A07206. https://doi.org/10.1029/2008JA013145

Erlandson, R. E., Mursula, K., & Bosinger, T. (1996). Simultaneous ground-satellite observations of structured Pc 1 pulsations. *Journal of Geophysical Research*, *101*, 27,149–27,156.

Ermakova, E. N., Kotik, D. S., Polyakov, S. V., & Shchennikov, A. V. (2007). On a mechanism forming a broadband maximum in the spectrum of background noise at frequencies 2–6 Hz. *Radiophysics and Quantum Electronics*, *50*, 555–569.

Fedorov, E., Mazur, N., Pilipenko, V., & Engebretson, M. (2016). Interaction of magnetospheric Alfvén waves with the ionosphere in the Pc1 frequency band. *Journal of Geophysical Research: Space Physics*, *121*, 321–337. https://doi.org/10.1002/2015JA021020

Fedorov, E., Mazur, N., Pilipenko, V., & Ermakova, E. (2016). Modeling diurnal variations of the IAR parameters. *Acta Geodaetica et Geophysica*, *51*, 597–617.

Feygin, F. Z., Nekrasov, A. K., Mursula, K., Kangas, J., & Pikkarainen, T. (1994). Coherent multiple Pc1 pulsation bands: Possible evidence for the ionospheric Alfvén resonator. *Annals of Geophysics*, *12*, 147–151.

Fraser-Smith, A. C. (1987). Narrow frequency bands in hydromagnetic emissions (Pc1). *Journal of Atmospheric and Solar-Terrestrial Physics*, *29*, 1541–1557.

Fraser, B. J., Loto'Aniu, T. M., & Singer, H. J. (2006). Electromagnetic ion cyclotron waves in the magnetosphere. In K. Takahashi, et al. (Eds.), *"Magnetospheric ULF waves: Synthesis and new directions", Geophysical Monograph Series* (Vol. 169, pp. 195–212). Washington DC: American Geophysical Union.

Fujita, S., & Tamao, T. (1988). Duct propagation of hydromagnetic waves in the upper ionosphere. 1. Electromagnetic field distributions in high latitudes associated with localized incidence of a shear Alfvén wave. *Journal of Geophysical Research*, *93*, 14,665–14,673.

Ginzburg, V. L. (1970). *The propagation of electromagnetic waves in plasmas*. New York: Oxford. Pergamon Press.

Greifinger, C., & Greifinger, P. (1968). Theory of hydromagnetic propagation in the ionosphere wave guide. *Journal of Geophysical Research*, *73*, 7473–7490.

Greifinger, C., & Greifinger, P. (1973). Wave guide propagation of micropulsations out of the plane of the geomagnetic meridian. *Journal of Geophysical Research*, *78*, 4611–4618.

Hayashi, K., Kokubun, S., Oguti, T., Tsuruda, K., Machida, S., Kitamura, T., et al. (1981). The extent of Pc 1 source region in high latitudes. *Canadian Journal of Physics*, *59*, 1097–1105.

Iyemori, T., & Hayashi, K. (1989). Pc 1 micropulsations observed by Magsat in the ionospheric F region. *Journal of Geophysical Research*, *94*, 93–100.

Keika, K., Takahashi, K., Ukhorskiy, A. Y., & Miyoshi, Y. (2013). Global characteristics of electromagnetic ion cyclotron waves: Occurrence rate and its storm dependence. *Journal of Geophysical Research Space Physics*, *118*, 4135–4150. https://doi.org/10.1002/jgra.50385

Kennel, C. F., & Petschek, H. E. (1966). Limit on stably trapped particle fluxes. *Journal of Geophysical Research*, *71*, 1–28.

Kikuchi, T., & Hashimoto, K. K. (2016). Transmission of the electric fields to the low latitude ionosphere in the magnetosphere-ionosphere current circuit. *Geoscience Letters*, *3*, 1–11. https://doi.org/10.1186/s40562-016-0035-6

Kim, H., Lessard, M. R., Engebretson, M. J., & Luhr, H. (2010). Ducting characteristics of Pc 1 waves at high latitudes on the ground and in space. *Journal of Geophysical Research*, *115*, 310. https://doi.org/10.1029/2010JA015323

Kim, H., Lessard, M. R., Engebretson, M. J., & Young, M. A. (2011). Statistical study of Pc1-2 wave propagation characteristics in the high-latitude ionospheric waveguide. *Journal of Geophysical Research Space Physics*, *116*, 227. https://doi.org/10.1029/2010JA016355

Kuwashima, M., Toya, T., Kawamura, M., Hirasawa, T., Fukunishi, H., & Ayukawa, M. (1981). Comparative study of magnetic Pc1 pulsations between low latitudes and high latitudes: Statistical study. *National Institute Polar Research Memoirs*, *18*, 101–117.

Lehtinen, N. G., & Inan, U. S. (2008). Radiation of ELF/VLF waves by harmonically varying currents into a stratified ionosphere with application to radiation by a modulated electrojet. *Journal of Geophysical Research*, *113*, A06301. https://doi.org/10.1029/2007JA012911

Leonovich, A. S., Mazur, V. A., & Senatorov, V. A. (1983). An Alfvén waveguide. *Zhurnal Eksperimental'noi i Teoreticheskoi Fiziki*, *85*, 141–145.

Lee, D.-H., Johnson, J. R., Kim, K., & Kim, K.-S. (2008). Effects of heavy ions on ULF wave resonances near the equatorial region. *Journal of Geophysical Research Space Physics*, *113*, A11212. https://doi.org/10.1029/2008JA013088

Lessard, M. R., & Knudsen, D. J. (2001). Ionospheric reflection of small-scale Alfvén waves. *Geophysical Research Letters*, *28*, 3573–3576.

Lyons, L. R., & Thorne, R. M. (1972). Parasitic pitch angle diffusion of radiation belt particles by ion cyclotron waves. *Journal of Geophysical Research*, *77*, 5608–5616.

Lysak, R. L. (1993). Generalized model of the ionospheric Alfvén resonator. In R. L. Lysak (Ed.), *"Auroral plasma dynamics", Geophysical Monograph Series* (Vol. 80, pp. 121–128). Washington, DC: American Geophysical Union.

Lysak, R. L. (1997). Propagation of Alfvén waves through the ionosphere. *Physics and Chemistry of the Earth*, *22*, 757–766.

Lysak, R. L., & Yoshikawa, A. (2013). Resonant cavities and waveguides in the ionosphere and atmosphere. In K. Takahashi, et al. (Eds.), *Magnetospheric ULF waves: Synthesis and new directions*. Washington, DC: American Geophysical Union.

Mann, I. R., Usanova, M. E., Murphy, K., Robertson, M. T., Milling, D. K., Kale, A., et al. (2014). Spatial localization and ducting of EMIC waves: Van Allen Probes and ground-based observations. *Geophysical Research Letters*, *41*, 785–792.

Mursula, K., Prikner, K., Feygin, F. Z., Braysy, T., Kangas, J., Kertulla, R., et al. (2000). Nonstationary Alfvén resonator: New results on Pc1 pearls and IPDP events. *Journal of Atmospheric and Solar-Terrestrial Physics*, *62*, 299–309.

Nomura, R., Shiokawa, K., Pilipenko, V., & Shevtsov, B. (2011). Frequency-dependent polarization characteristics of Pc1 geomagnetic pulsations observed by multipoint ground stations at low latitudes. *Journal of Geophysical Research*, *116*, A01204. https://doi.org/10.1029/2010JA015684

Ostapenko, A. A., & Polyakov, S. V. (1990). Dynamics of the reflection coefficient of Alfvén waves in Pc1 range during variations of the bottom ionosphere electron concentration. *Geomagn Aeronomy*, *30*, 50–56.

Pilipenko, V. A. (2012). Impulsive coupling between the atmosphere and ionosphere/magnetosphere. *Space Science Review*, *168*, 533–550.

Pilipenko, V., & Heilig, B. (2016). ULF waves and transients in the topside ionosphere. In A. Keiling, D. H. Lee, & V. Nakariakov (Eds.), *"Low-frequency waves in space plasmas", Geophysical Monograph 216* (pp. 15–29). Hoboken: Wiley/AGU.

Potapov, A., Polyushkina, T., Afraimovich, E., Lipko, Y. u., & Hayashi, K. (2002). Transequatorial propagation of the Pc1 emission on 23 October 1997. *Journal of Geophysical Research*, *107*, 1128. https://doi.org/10.1029/2001JA000225

Potapov, A. S., Polyushkina, T. N., Dovbnya, B. V., Tsegmed, B., & Rakhmatulin, R. A. (2014). Emissions of ionospheric Alfvén resonator and ionospheric conditions. *Journal of Atmospheric and Solar-Terrestrial Physics*, *119*, 91–101.

Prikner, K., Mursula, K., Kangas, J., & Feygin, F. Z. (2001). Ionospheric Alfvé,n resonator control over the frequency-variable Pc1 event in Finland on May 14, 1997. *Studia Geophysica et Geodaetica*, *45*, 363–381.

Prikner, K., Mursula, K., Kangas, J., Kerttula, R., & Feygin, F. Z. (2004). An effect of the ionospheric Alfvén resonator on multiband Pc1 pulsations. *Annales Geophysicae*, *22*, 643–651.

Shprits, Y. Y., Subbotin, D. A., Meredith, N. P., & Elkington, S. (2008). Review of modeling of losses and sources of relativistic electrons in the outer radiation belt II: Local acceleration and loss. *Journal of Atmospheric and Solar-Terrestrial Physics*, *70*, 1694–1713.

Surkov, V., & Hayakawa, M. (2014). Ultra and extremely low frequency electromagnetic fields, Springer geophysics series, XVI. Japan.

Ukhorskiy, A. Y., Shprits, Y. Y., Anderson, B. J., Takahashi, K., & Thorne, R. M. (2010). Rapid scattering of radiation belt electrons by stormtime EMIC waves. *Geophysical Research Letters*, *37*, L09101. https://doi.org/10.1029/2010GL042906

Woodroffe, J. R., & Lysak, R. L. (2012). Ultra-low frequency wave coupling in the ionospheric Alfvén resonator: Characteristics and implications for the interpretation of ground magnetic fields. *Journal of Geophysical Research*, *117*, A03223. https://doi.org/10.1029/2011JA017057

Yagova, N., Pilipenko, V., Fedorov, E., Vellante, M., & Yumoto, K. (1999). Influence of ionospheric conductivity on mid-latitude Pc3–4 pulsations. *Earth Planets and Space*, *51*, 129–138.

Yahnin, A. G., Yahnina, T. A., & Frey, H. U. (2007). Subauroral proton spots visualize the Pc1 source. *Journal of Geophysical Research*, *112*, A10223. https://doi.org/10.1029/2007JA012501